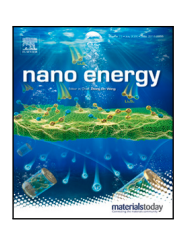


Contents lists available at ScienceDirect

Nano Energy

journal homepage: www.elsevier.com/locate/nanoen



Full paper

Micro-triboelectric generator for zero-power shock detection

Mohammad Alzgool a, Mohammad Mousavi a, Benyamin Davaji b, Shahrzad Towfighian a,*

- ^a Binghamton University, 4400 Vestal Parkway East, Binghamton, NY 13902, United States of America
- ^b Northeastern University, 360 Huntington Ave, Boston, MA 02115, United States of America

ARTICLE INFO

Keywords: Tribo-electric-nano-generator MEMS Shock sensing Actuators Self-powered Energy harvester

ABSTRACT

This work shows zero-power shock sensing for the combination of a micro-triboelectric generator and MEMS electrostatic actuator system where the mechanical shock to the generator causes it to produce voltage, this voltage is used to actuate a Micro-Electro-Mechanical-system (MEMS) switch. For the first time, we present the fabrication process of a Triboelectric-Nano-Generator (TENG) with MEMS technology. The MEMS-TENG has a suspended 1.5 mm \times 1.5 mm plate separated by 2 μ m from the substrate. The generator is a triboelectric transducer made of a suspended Al micro-plate above a polyimide (PI) thin layer that is covered by another Al layer in the back. In case the shock is sufficiently strong, the micro-plate hits its substrate. As a result of the impact, electrification happens and PI gets negatively charged, while the Al gets positively charged. Connecting the generator to a MEMS switch, we use the generated voltage to actuate a MEMS switch. The TENG was able to supply voltage difference up to 0.4 V at 2.3g. We use the MEMS-TENG to actuate a cantilevered MEMS switch (500 \times 20 \times 2 μ m) separated by a 2 μ m gap from a fixed bottom electrode. Triboelectric generators are known for high voltages and low currents, which makes them ideal for integration with MEMS electrostatic devices that require ultra-low power to operate. Our feasibility study opens doors to billions of innovative devices that can be created from this synergistic combination.

1. Introduction

Nowadays, the focus of research on energy harvesting is increasingly aiming to use environmental energy. Energy harvesting is important for powering sensors and actuators, especially for devices of the Internet of Things (IoT). The IoT is a network of nodes where each node contains sensors and a connection to a person or a thing, and it is the main pillar of a smart city [1].

The development of IoT comes with the challenge of providing enough power. By the end of 2025 there will be more than 50 billion devices connected to the IoT. To meet the power requirement, researchers have studied several energy harvesting methods such as liquid–solid electrical double layer [2], electromagnetic [3–6], magnetoelectric [6] pyroelectric [7], chemical [8], electrostatic [9], piezoelectric [10–15], triboelectric [16–27], and hybrid energy harvesters which employ piezo-electric harversters (PEHs) or tribo-electric-nanogenerators (TENGs) together or with other types of harvesters [3,5,12, 28–30].

The Electro-static harvesters are used to collect mechanical energy. They generate power from mechanical excitation, and the generated power can drive low-power sensors [31], the generator has pre-charged plates that avoid touching due to the presence of a spacer in-between,

a similar type of non-contact design with proof-mass was presented to tune the resonance frequency for the generator [32]. On the other hand, a contact-mode electrostatic harvester was made in a rotary mode [33]. This type of generator was presented and studied in the micro-scale [34, 35]. The resulting high-frequency resonance in MEMS-scale devices improves the efficiency of harvesting the energy of impacts.

The piezoelectric energy harvesters collect mechanical energy by taking advantage of the embedded piezoelectric material such as Zinc Oxide (ZnO), Lead Zirconate Titanate (PZT), and Polyvinylidene fluoride (PVDF) [36], PEHs are used in several applications including rain energy harvester REH [37], ambient energy to power sensors and chips [13], wearable electronics [28,36,38–40], wind energy [10,41], biomechanical energy harvesting [28,36].

Mechanical energy can be harvested using Triboelectric-Nano-Generators (TENGs) when two materials with different affinities for gaining or losing electrons contact and separate as in Contact-Separation mode harvesters (C-S) [23]. The most common triboelectric materials are Polytetrafluoroethylene (PTFE), Polyimide (PI) and Poly-dimethylsiloxane (PDMS) [22]. Other triboelectric materials that are used include hydroxyethyl cellulose [21], patterned SU8 [20], fluorinated ethylene propylene [17], protein-based [42], paper-based [24],

E-mail addresses: malzgoo1@binghamton.edu (M. Alzgool), smousav1@binghamton.edu (M. Mousavi), b.davaji@northeastern.edu (B. Davaji), stowfigh@binghamton.edu (S. Towfighian).

^{*} Corresponding author.

and molecularly engineered tribo-material [43]. Applications for TENGs are widespread, for instance, they are used in wind energy [21, 26,44], wearable electronics [22], human-motion [25,28,45], blue energy [3], harvesting energy from moving cars' exhaust and tires [16, 17], powering sensors to detect vibration, temperature, and displacement [3,19,27], and for pressure and strain as in artificial skins [23].

Research on TENGs is growing because of their advantages such as relatively low cost, flexibility, high output, easy fabrication, costeffectiveness, long-term durability, and their ability to be integrated into systems [46]. These advantages allow TENGs to be used to create self-powered sensors. Applications include carbon nanotubes with PDMS as an independent power source to monitor changes in human body motion [12]. Another example is the interaction of a motion-information sensor with TENGs with an array of PDMS/PTFE acts as the triboelectric layer [18]. The triboelectric property was used to drive a filter with a triboelectric-electrostatic field [17]. TENGs in car tires were suggested as a possible independent power supply for electronic sensor [16]. TENGs were integrated with a wearable electronics application as a power supply for low-power consumption passive electronics by harvesting human motion [22,25,36,47]. Moreover, TENGs are used as the power source for independent pressure sensors [23], temperature sensors, [26,27], and vibration sensors [5]. While many studies focused on triboelectric materials, investigations on the integration of TENG with MEMS are sparse. The advantages of MEMS sensors and actuators such as their low-power requirements, small sizes, and advanced functionalities [48] make TENGs and MEMS a functional pair. We studied this combination using a macro size bi-stable TENG and a micro-cantilevered beam to create a shock sensor [49,50].

To miniaturize the sensing and actuation platforms, it is essential to make micro-scale generators. However, the dimensions of conventional TENGs were commonly in the centimeters range, for instance, an ambient energy harvester reported by Yingchun et al. [26] has 67 mm in length, 22 mm in width, and 10 mm in thickness. The TENG sheets suggested for car tires are $120 \times 110 \times 30 \text{ mm}^3$ in dimensions [16]. There have been a few attempts to make TENG at a microscale. For example, Chen et al. [51] made a micro TENG with a large top electrode shaped as micro-patterned circles that are 50 µm in diameter and are made of gold with a gap of 90 nm, all the circles were connected in parallel like a net. The fabrication of this device requires wafer bonding to create a sealed vacuum gap under the membrane. This device is presented as an ultrasonic transducer working in the megahertz frequency and generates a maximum of 17 mV at 1 MHz. Another design for smaller devices was made by Hamid et al. [52] where the designed TENG was 3 mm × 5 mm, this design used PTFE as triboelectric material combined with Aluminum and gold, an $8.5~\mu m$ thick layer of nickel was deposited on top of aluminum to serve as proof mass, and the gap between triboelectric layer and top layer was 13 μm in this design. This design was implemented by Hamid et al. [53] with UV-LIGA technology which makes packaging and integration with other components difficult.

In this work, we will demonstrate fabrication of MEMS-TENG made in a microfabrication Facility with length and width of 1.5 mm and thickness of $\sim\!\!1.10~\mu m$, the triboelectric layer considered in this work was PI, top and bottom conductive layers are both aluminum, and proof mass of amorphous-Silicon. The superior property of our approach is its smallest size for TENG and its compatibility with CMOS-fabrication for integration with electronic components. The fabricated shock detector can be used for shipment monitoring devices or in the inner layer of helmets for athletes to detect if shocks they encounter exceed a threshold.

2. Design and fabrication of the MEMS-TENG

TENGs are generally composed of three layers, two conductive layers and a triboelectric layer on one of them, separated by a gap. When conductive and triboelectric layers are in contact, the different

affinity for gaining or losing electrons causes each side to gain an electric charge but with an opposite polarity, which results in a voltage difference.

Fabrication (Fig. 1) starts with depositing 1.5–1.7 μm of Aluminum Nitride (AlN). AlN was selected because of its enhanced etch selectivity (etch stop layer) which will be key for the following steps. The bottom conductive layer is then formed by DC-magnetron sputtering. Chromium (Cr) is sputtered for 210 s at a pressure of 7 mtorr followed by sputtering of Al for 1235 s at the same pressure (Fig. 1a). The Cr layer improves the stiction of the Al layer to the wafer. The sputtering results in \sim 20 nm of Cr and 200 nm of Al. Then, the Cr/Al layer is patterned using Mask L1 and Inductive-Conductive-Plasma (ICP) (Fig. 1b). The etching was done under BCl₃, Cl₂, Ar, and CH₄ gases for \sim 5 min with SPR220-3.0 positive photoresist. Removal of the photoresist is done with a 2–5 min ashing recipe. Al was chosen for both electrodes because it is easy to deposit, etch, and the resulting film stress is controllable.

Then, a Polyimide precursor (PI2574-HDmicrosystems) is spun at 5000 rpm onto the Cr/Al for 30 s. The wafer was then baked on a hot plate for 30 s at 120 °C followed by 30 s bake at 150 °C, the wafer is then baked in a PI oven for 30 min under 200 °C followed by a 1-hour bake under 300 °C, and the baking process results in ~4.7 µm thick PI (Fig. 1c). For PI patterning, we used photolithography done with a Mask L2 with a Reactive-Ion-Etching machine (RIE) (Fig. 1d). This step was run with an aggressive recipe of CF₄:O₂ that had a 1:4 ratio of the gases in the RIE machine [54], the pressure was set to 90 mtorr. The power was set to 200 Watts. The etching time was ~15 min but it was run for 9 min followed by steps of 3 min to ensure the photoresist layer was not removed. Because of the low selectivity of this recipe to the photoresist, SPR220-7.0 photoresist was chosen instead of SPR220-3 to conduct the photolithography on the PI. Removing this photoresist after completion cannot be done with ashing because it will attack photoresist and Polyimide layers. Instead, the wafer was submerged into a Microposit 1165 photoresist remover solution for a day and then washed with Isopropynol solution.

After patterning the PI, a 2µm Plasma-Enhanced-Chemical-Vapor-Deposition (PECVD) film of ${\rm SiO}_2$ is deposited using a high-rate recipe (Fig. 1e). The layer was patterned and etched using the photolithography Mask L3 and RIE machine. We used SPR220-3.0 photoresist and a recipe of 45 sccm CHF $_3$ and 15 sccm Ar at 50 mtorr and power of 200W for ~50 min. That recipe is very selective but moderately slow as it etches ~33 nm/min (Fig. 1f). For the pins, photolithography Mask L4 was used with a CHF $_3$ /O $_2$ recipe in RIE. The pins were 1 µm thick. The etching was done for 20 min resulting in ~0.8 µm pins (Fig. 1g). These pins are included in the design to increase surface area and, therefore, increase the friction between the layers.

On top of the sacrificial layer, Cr is sputtered for 150 s followed by Al for 1000 s at 5 mtorr. The pressure was chosen to control film stress. At 5 mtorr, film stress is relatively low and the deposition rate is relatively high (Fig. 1h). The resulting Cr/Al film was around 100 nm thick and has 20–60 MPa Compressive stress. That layer was patterned using a photolithography Mask L5 with an ICP machine using the same recipe that was used for the bottom electrode to create the top electrode, but without the release holes (Fig. 1i).

The last film deposited onto the top electrode is the a-Si proof mass. Its recipe was manipulated to keep the resulting stress Tensile and below 180 MPa to avoid breaking after release. The best conditions for that purpose were found to be using °C 200 and 2 torr pressure and a low-frequency power parameter set to 20 Watts. The resulting stress was $\sim\!100$ MPa tensile. Deposition under these parameters for 30 min results in about $\sim\!1$ µm thick a-Si (Fig. 1j). Photolithography Mask L6 and RIE were used for patterning the a-Si to open contacts (wiring pads). The RIE recipe consists of a SF₆/O₂ mixture for isotropic silicon etching and the photoresist was SPR220-3.0 as the recipe selectivity for a-Si is high, this recipe is also very fast and only 2 min were required to remove the a-Si and open the contacts (Fig. 1k). After opening

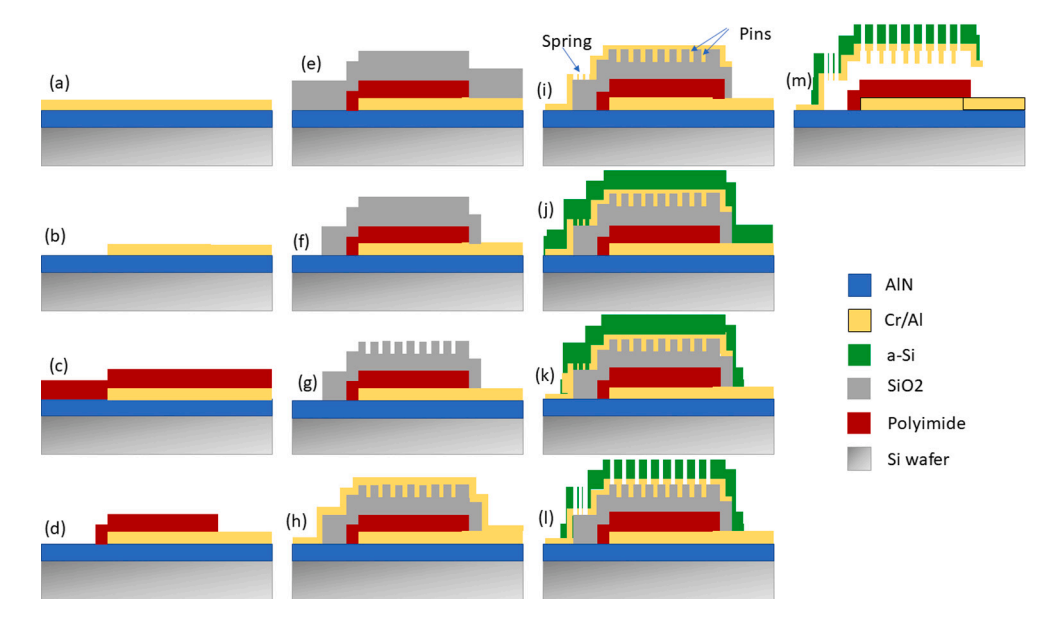


Fig. 1. MEMS-TENG fabrication process flow where (a) Sputtering Cr/Al, (b) Patterning Cr/Al bottom electrode, (c) Spin-coating polyimide, (d) Patterning polyimide, (e) SiO₂ PECVD film deposition, (f) Patterning SiO₂ film, (g) Pins pattern/mold etching on SiO₂ film, (h) Sputtering of Cr/Al top electrode, (i) Patterning of Cr/Al top electrode, (j) Deposition of PECVD a-Si film, (k) Contact opening, (l) Patterning top electrode with release holes, (m) Top electrode release.

contacts, both proof-mass (a-Si) and the conductive layer (Cr/Al) on top are etched again to form the proof-mass layer and the release holes. This step is conducted by photolithography Mask L7 and RIE (for a-Si) followed by ICP (for Cr/Al). The same parameters were used as in steps (i) and (k).

After patterning the top layer, the wafer is diced using dicing saw and inserted into vapor Hydrogen-Fluoride (vHF) to remove the sacrificial SiO₂. The process takes 1.5-2 h (Fig. 1m). A released MEMS-TENG is shown in Fig. 2.

The MEMS-TENG fabrication process implemented in this paper is simpler than the process developed by Hamid et al. [53] where the UV-LIGA technique was used. In this work, the top electrode was fabricated with a combination of sputtered Cr/Al films and a PECVD film of a-Si whereas in the work of Hamid et al. [53] the top electrode was formed by sputtering Al and electroplating of gold (Au) and nickel (Ni). The advantage of this process over the PECVD is that the top electrode is composed of conductive materials while in our work the top electrode is made of a conductive Al layer and a non-conductive a-Si, beside the effect it might have on the resulted MEMS-TENG electrical performance, it also made it necessary to add a mask for contactopening to our design. The sacrificial layer used in this work is a SiO2 PECVD film. The film can be removed with vHF in 90-120 min while the sacrificial layer in the work of Hamid et al. [53] was made of a photodefinable PI that has to be ashed for 800 h in high-pressure O₂ plasma to ensure full removal. Fig. 3 shows our fabricated device. The figure shows a top view, a close-up view of the top electrode, and SEM images for the fabricated device pins and the release holes.

The fabrication described in Fig. 1 requires 7 photomasks (Mask L1–Mask L7) for steps b, d, f, g, i, k, and l. These masks were drawn on AutoCAD software and exported to KLayout. The design is shown in Fig. 2 with a 3D schematic of the generator. The design has a square top electrode with 1.5 mm sides, spring turns were made after a MEMS-accelerometer design [55]. The turns are 40 $\mu m \times 90~\mu m$; the width of the spring is 30 $\mu m \times 15~\mu m$ as shown in Fig. 2 and Table 1.

3. Modeling and simulation

Modeling the mechanical motion and electrics of the MEMS-TENG are investigated in this section. Consider a micro-plate connected to four springs as depicted in Fig. 2b. The surface area of the plate is

Table 1
Dimensions of the Micro-sized-TENG.

Parameter	Symbol	Value
Side Length	L	1500 μm
Bottom electrode thickness	t_{BE}	200 nm
Triboelectric layer thickness	t_T	5 μm
Gap	d	2 μm
Top electrode thickness	t_{TE}	100 nm
Proof mass thickness	t_{PM}	1 μm
Vacuum permittivity	ϵ_0	8.85×10^{-12} F/m
Dielectric constant	ϵ_r	3
Spring dimensions	α_1	30 μm
Spring dimensions	α_2	45 μm
Spring dimensions	α_3	40 μm
Spring dimensions	$lpha_4$	90 μm
Spring dimensions	α_5	15 μm
Damping coefficient	c	0.0001 N s/m
Impact damping	c_i	0.001 N s/m
Impact stiffness	$\vec{k_i}$	1.5 N/m

denoted by S; the gap between the plate and substrate is denoted by d; the fundamental frequency of the out-of-plane motion is $f_0 = 0.8$ kHz; and the total mass of the plate is m. The damping force is modeled as a linear damper which was obtained using the logarithmic decrement method and experimental results. The squeeze film damping is not considered in this model because as described in Section 2, the MEMS-TENG movable electrode contains arrays of holes (see Fig. 3) and noticeably prevents air trapping between the movable electrode and polyimide. The experiments show that the linear damping approximation gives proper estimation. The charge generation between the triboelectric layers is modeled according to [56,57] as:

$$\dot{q} = \frac{V_{gen}}{R} = -\frac{q}{\epsilon_0 SR} (\frac{t_T}{\epsilon_r} + d - z) + \frac{\sigma}{\epsilon_0 R} (d - z) \tag{1}$$

The parameters of Eq. (1) [58] are available in Table 1. The generated charge is a function of the penetration of the layers. $S = L^2$ is the MEMS-TENG top electrode surface area.

The penetration of the triboelectric layers is calculated in Eq. (2) as the difference between the plate displacement and the initial gap d (see Fig. 2b).

$$\delta = z - d \tag{2}$$

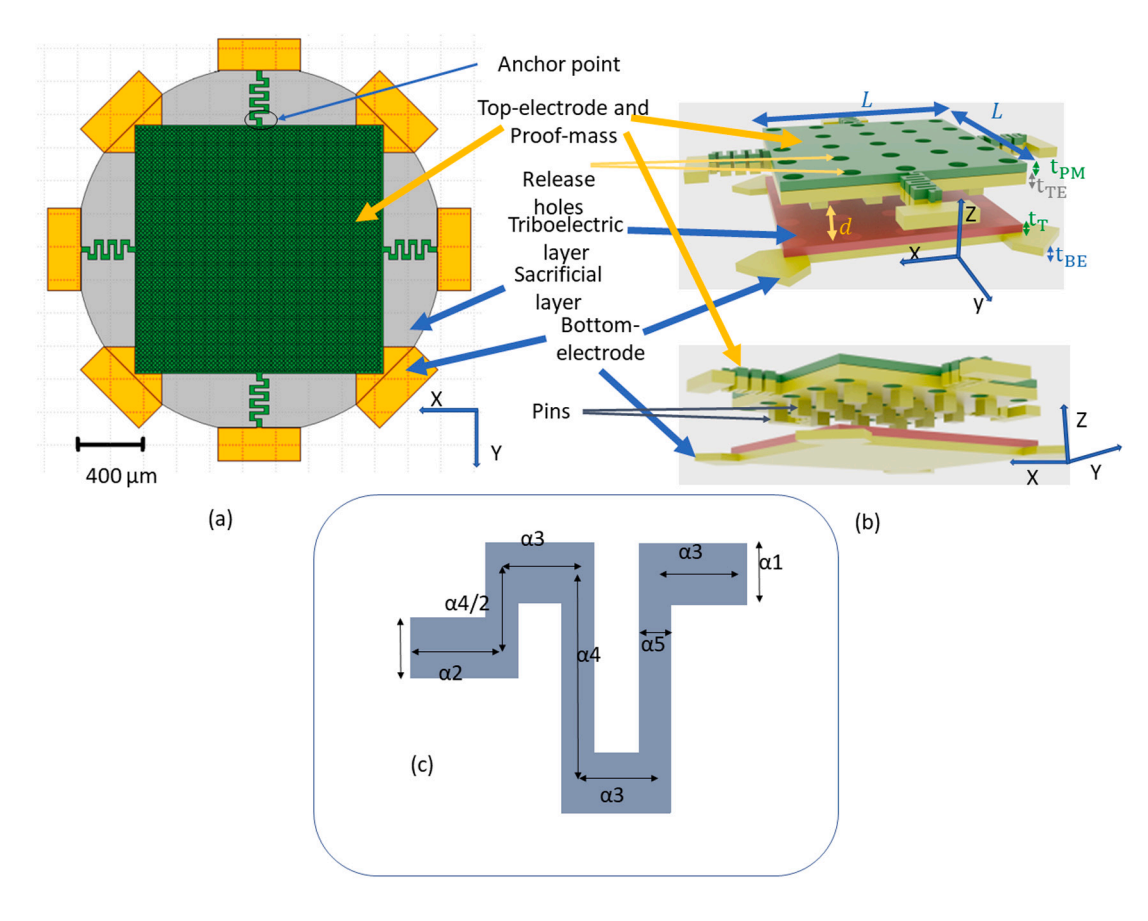


Fig. 2. (a) Top view of MEMS-TENG design layout in KLayout design environment, (b) 3D schematic of the MEMS-TENG, (c) illustration of the microspring layout dimensions.

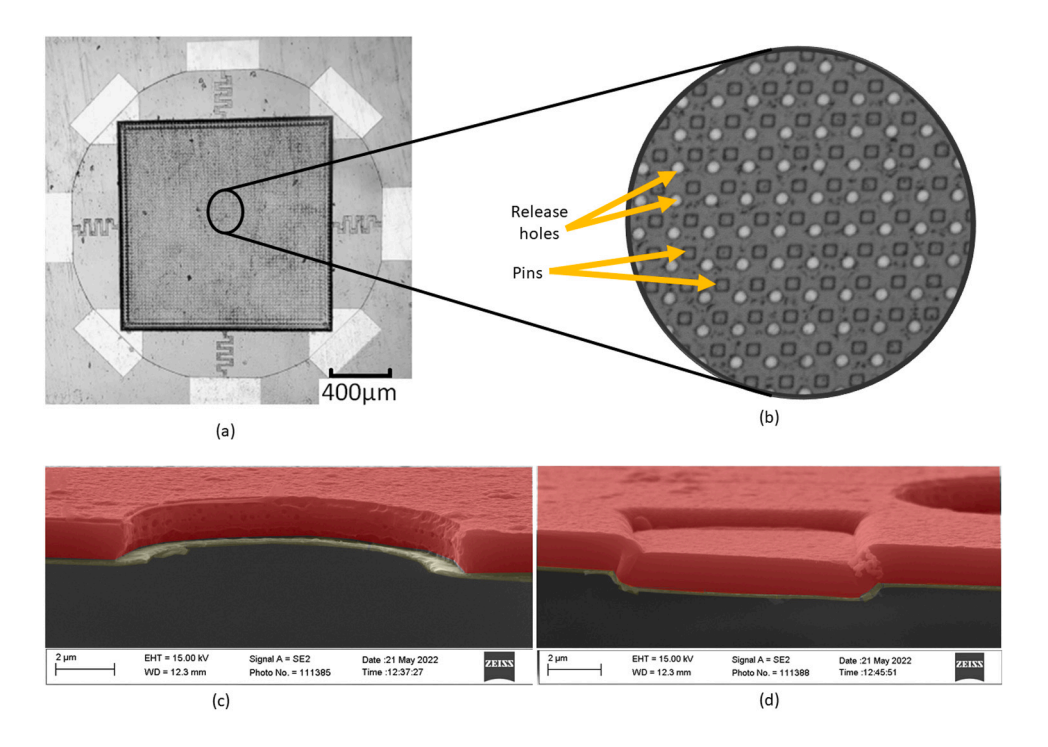


Fig. 3. The fabricated MEMS-TENG where (a) is the top view from a microscope, (b) is a closer look at the top view, circles are holes needed for the release step, and squares are the pins in the top layer, (c) and (d) are SEM images of release holes (circles) and pins (squares), respectively. a-Si layer is highlighted in red and Al electrode is highlighted with yellow in false-colored SEM images.

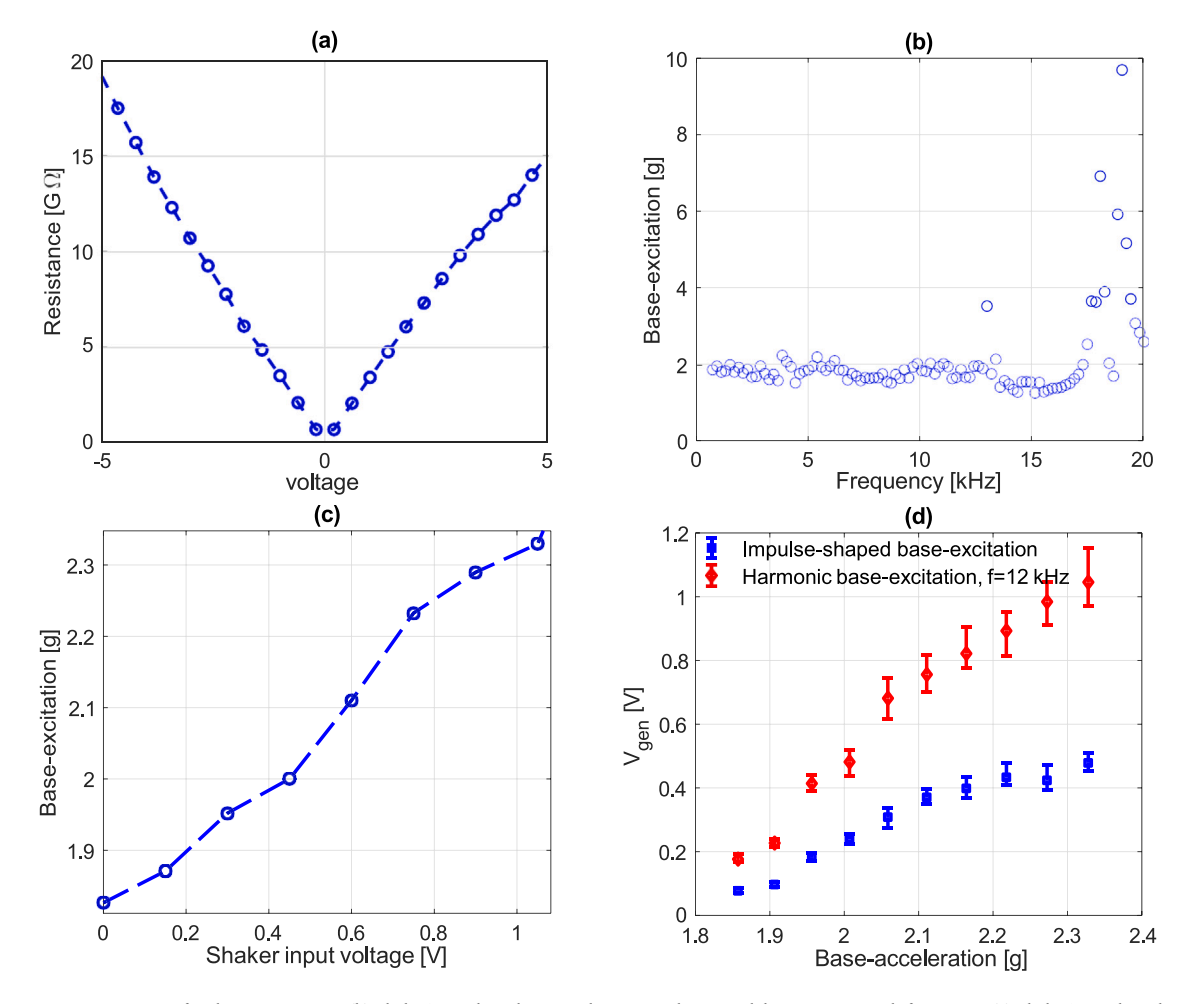


Fig. 4. (a) Resistance measurement for the MEMS-TENG, (b) Shaker's resulting base acceleration with sinusoidal 0.5 V input with frequency, (c) Shaker's resulting base acceleration with varying input voltage, at f = 12 kHz (d) MEMS-TENG's peak to peak output voltage against varying base-acceleration.

A large spring and damping force models the impact force as

$$F_{impact} = -c_i \dot{\delta} - k_i \delta \tag{3}$$

Eq. (3) is activated while the layers are in contact. The values for $c \approx 10^{-4}$ N s/m, $c_i \approx 2 \times 10^{-4}$ N s/m, and $k_i = 1.5$ N/m are selected according to the experimental time–history of the MEMS-TENG. The second force applied to the movable electrode is the electrostatic force between the electrodes is modeled. The capacitance is calculated as

$$C(z) = \frac{\epsilon_0 S}{d - z} \tag{4}$$

The electrical potential stored between the electrode is

$$U = \frac{1}{2}C(z)V^2 \tag{5}$$

Considering the capacitance in Eq. (4), and the fact that V=q/C(z), the electrostatic force can be calculated as

$$F_{elec} = \frac{\partial U(V,z)}{\partial z} = \frac{q^2}{2\epsilon_0 S} \tag{6}$$

The frequency response of the generator shows that the fundamental frequency of the transverse motion is approximately 0.8 kHz. Considering the mass of the movable electrode which is $m = 5.85 \times 10^{-9}$ indicates that the stiffness of the device springs together is 0.1478 N/m.

The dynamics of the generator are modeled with a linear spring-mass-damper system with external forces Eq. (3), (6) that is prone to impact and electrostatic forces as in Eq. (7).

$$m\ddot{z} + c\dot{z} + 4\pi^2 f_0^2 \ mz = F_{impact} + F_{elec}(q) - ma(t)$$
 (7)

Eqs. (1)–(7) will be used to simulate the out of the MEMS-TENG generator that closes a MEMS-switch when a shock is strong enough.

4. Results and discussion

4.1. Resistance measurement

The fabrication process of the MEMS-TENG started with a deposition of an insulating layer to ensure no current leakage occurs between top and bottom conductive electrodes, the measurement of resistance between both electrodes was conducted using Keithley SourceMeter 2636B where it applies voltage and calculates resistance from resulting current. The measured resistance is shown in Fig. 4a.

The high resistance resulting from the resistance measurement means that the AlN layer in the fabricated MEMS-TENG which acts as an insulating layer was successful in minimizing the leakage of current that would occur if the device were built directly on the Silicon wafer. We notice the measured resistance falls in the range of 600 $M\Omega$ - 20 G Ω when voltage difference of -5 to +5 V is applied, and a current in the range of 0.2–0.3 nA is passed. The applied voltage decreases the gap leading to an increase in the parasitic resistance.

4.2. MEMS-TENG testing

To test the voltage generation of the MEMS-TENG, it was mounted on a mini-shaker for controlled and open-circuit voltage was measured. The transfer function of the electrodynamic mini-shaker was tested.

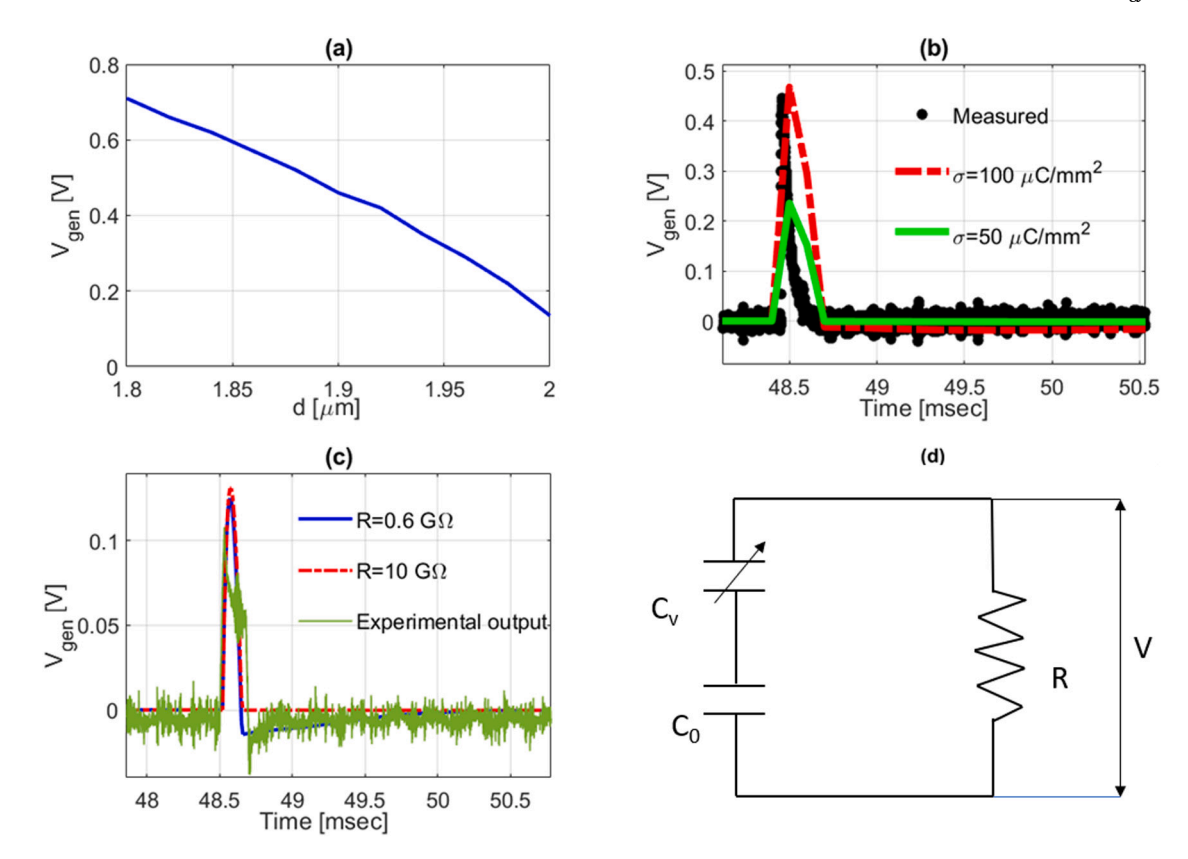


Fig. 5. Simulation results for a MEMS-TENG actuated by impulse shock. (a) the effect of the initial gap between the MEMS-TENG electrodes on the generated voltage. A shock acceleration of 2.2g is considered. (b): measured and simulated time response for different charge densities. The initial gap and resistance are considered $d = 1.9 \, \mu m$ and $R = 0.6 \, G\Omega$. (c): Simulation results for the comparison of different MEMS-TENG electrical resistances prone to impulse base-excitation. The base acceleration of 2g, the initial gap of $d = 2 \, \mu m$, the charge density of $\sigma = 100 \, \frac{\mu C}{mm^2}$ are considered in the results of this figure. (d) Simplified electrical schematic of the MEMS-TENG.

The acceleration of the shaker's dock was measured using the Laser-Doppler-Vibrometer with a constant AC voltage (V_{AC}) and the input frequency was swept. Fig. 4b shows a uniform acceleration of 2.1g in the range of 70 Hz–16 kHz with $V_{AC}=0.5$ V. The reliable range for the frequency response of the MEMS-TENG based on our measurement capability is discussed as follows. The shaker was used to test against different input AC voltages with a fixed frequency of 12 kHz with the acceleration ranges from 1.8 to 2.4 g as shown in Fig. 4c. Then, the response of the triboelectric generator is measured to different base excitation. The peak-to-peak open-circuit voltages are shown in Fig. 4d. The output varied from 0.2 to 1.1 V_{p-p} and the sensitivity is 1.5 V/g.

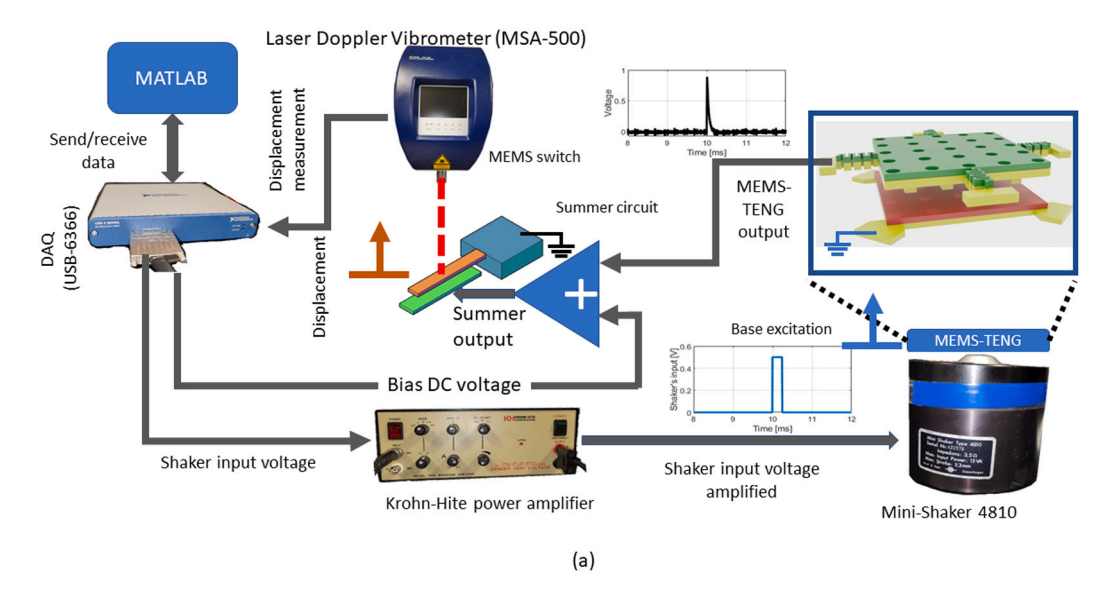
Table 2 compares the device's output with the state-of-the-art. The most important aspects to compare are the output voltage and the size of the device. TENGs are widely built in meso-scale [20,59,60]. Those sizes are adequate for energy harvesting from low-frequency vibration. The smallest TENG in the literature is fabricated with the UV-LIGA technique by Hamid et al. [53]. The electrodes fabricated in our work are in the same order of length and width as reported in Hamid et al.'s work (in mms). However, their work reported a wider range of sensitivity against the input acceleration (up to 9.33g). The major difference between our work and theirs is the thickness of the proof mass. We deposited ~1 µm of a-Si while in their work the proofmass was 10 µm of Ni. We used an Al and PI triboelectric pairing as opposed to their Al and Teflon. In our design, we used 2 µm gap inbetween the triboelectric pair while in Hamid et al.'s work they used a 13 µm gap that increased to 24 µm because of bowing after release. Their use of large sacrificial layer makes fabrication more expensive and cumbersome.

For the physical analysis and characterization of the MEMS-TENG, the results of the model in Section 3 are presented in the following. The simulation and experimental results appear in Fig. 5. The charge $\frac{1}{2}$

density, the TENG electrical resistance, and the initial gap between the polyimide and the top electrode are three uncertain parameters in Eq. (1) that affects the simulation outcomes. Firstly, the effect of the initial gap is illustrated in Fig. 5a. By reducing the gap between the top electrode and the polyimide, the generated voltage is significantly increased as a result of the larger impact force between the layers. The initial gap was set to $d=2~\mu m$ during the fabrication process. However, the top electrode curves after release because of residual stresses. The existence of $\sim 1~\mu m$ -tall pins means the gap between the electrodes is not uniform, which justifies the use of 1.9 μm that has a close agreement with simulation results.

Secondly, the charge density effect on the simulation was studied. By using the experimental results for the base acceleration of $a_{base}=2.2g$, charge density values used in the simulation were $\sigma=100~\frac{\mu C}{m^2}$ and $\sigma=50~\frac{\mu C}{m^2}$ to show its variation effect on the generated voltage. Similar to reported value in [58], the result of simulation when charge density is $\sigma=100~\frac{\mu C}{m^2}$ had close results to our experimental results for generated voltage from the MEMS-TENG.

Thirdly, the effect of electrical contact resistance (R) on the generated voltage was studied. We have measured the resistance for different DC voltages between the TENG electrodes (Fig. 4a). The figure shows how R ranges from $R=0.6~\rm G\Omega$ to $R=5~\rm G\Omega$. The result of the simulation show that the resistance does not have an important role in the maximum open-circuit generated voltage as shown in Fig. 5c. As the resistance vary, the generated positive impulse-shaped voltage is followed by a small negative peak when the resistance is $0.6~\rm G\Omega$ while the bigger resistance value of $10~\rm G\Omega$ does not show this negative peak, the profiles of the generated voltage are depicted in Fig. 5c. Because of the observed negative value of voltages (which was measured -0.02 V), the resistance is estimated to be around $0.6~\rm G\Omega$. The reason for negative voltage can be explained from a simple electrical circuit equivalent of



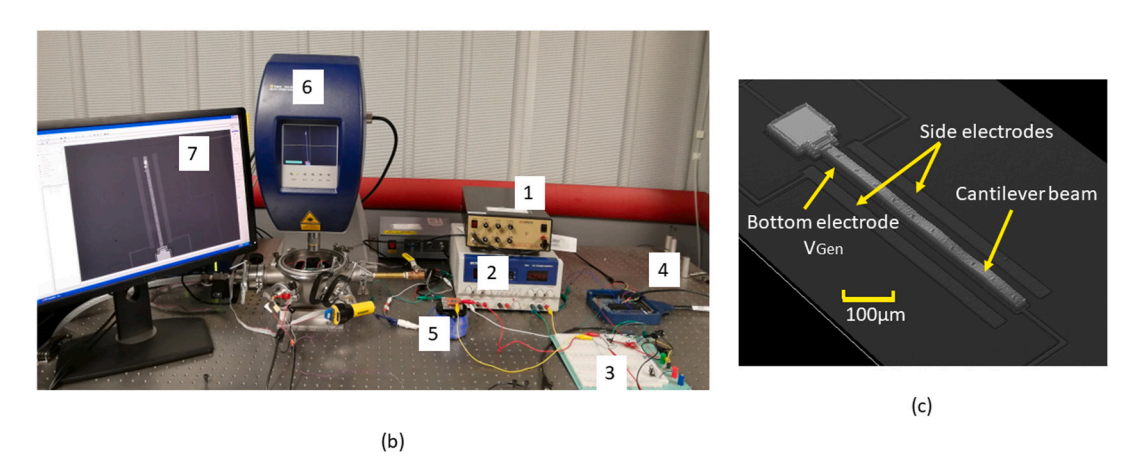


Fig. 6. (a) Schematic of the experimental setup for the combination of MEMS-TENG and MEMS-switch system, (b) Experimental setup for the MEMS switch actuation with MEMS-TENG, and (c) MEMS-Switch under the optical profiler (WYKO NT1100). The shown side electrodes are used to release the beam after pull-in.

the generator. In fact, the model of the generator is a variable capacitor (because of air gap change) in series with a fixed capacitor (because of the dielectric) and a leakage resistor. Using the simplified electrical model shown in Fig. 5d, the output voltage will be

$$V = \frac{Q}{C} \tag{8}$$

where Q is the charge and C is the total capacitance. The derivative of Eq. (8) with respect to time will yield

$$\frac{dV}{dt} = \frac{1}{C^2} \left(C \frac{dQ}{dt} - Q \frac{dC}{dt} \right) \tag{9}$$

which indicate the rate of change of voltage across the resistor. The simplified model for discharging in RC circuit is expressed as

$$Q(t) = Q_0 e^{-t/RC} \tag{10}$$

The derivative of charge with respect to time from Eq. (10) will be

$$\frac{dQ(t)}{dt} = \frac{-1}{RC}Q_o e^{-t/RC} \tag{11}$$

The combination of Eqs. (9) and (11) will give rate of change of voltage

$$\frac{dV}{dt} = \frac{-1}{RC^2} Q_o e^{-t/RC} - \frac{Q}{C^2} \frac{dC}{dt}$$
 (12)

When the generator is exposed to half sine excitation and when the two electrodes go away from each other, the change in the capacitance $(\frac{dC}{dt})$

will be negative making the second term positive and more dominate and increases the voltage. When the two electrodes approach each other in the second portion of the half sine, $\frac{dC}{dt}$ will be positive making the second term negative and the slope of voltage is negative. If the resistance is low, the negative slope of voltage ultimately causes the negative value for voltage as observed in Fig. 5c. If the resistance is too high, the effect of first term is almost negligible and the voltage may not become zero as observed in the simulations.

Although top electrode motion cannot be measured when the shaker is operating, the shape of the generated voltage in Fig. 5c is identical to the shape of typical triboelectric voltage generated in our previous works based on contact-separation [49], which indicates contact between upper electrode and PI. Based on our mesoscale triboelectric generator experiment, if contact does not happen, the voltage signal will be buried in noise.

4.3. MEMS switch actuation using MEMS-TENG

For this purpose, we made the experimental setup illustrated in Fig. 6a and b. A power amplifier (Krohn-Hite 7600) is used to drive the electro-dynamic shaker (mini-shaker 4810) because the current needed for its operation cannot be provided directly by the Data Acquisition System (DAQ), The MEMS-TENG was mounted on a mini-shaker operated using an amplified signal from the DAQ (USB-DAQ 6366).

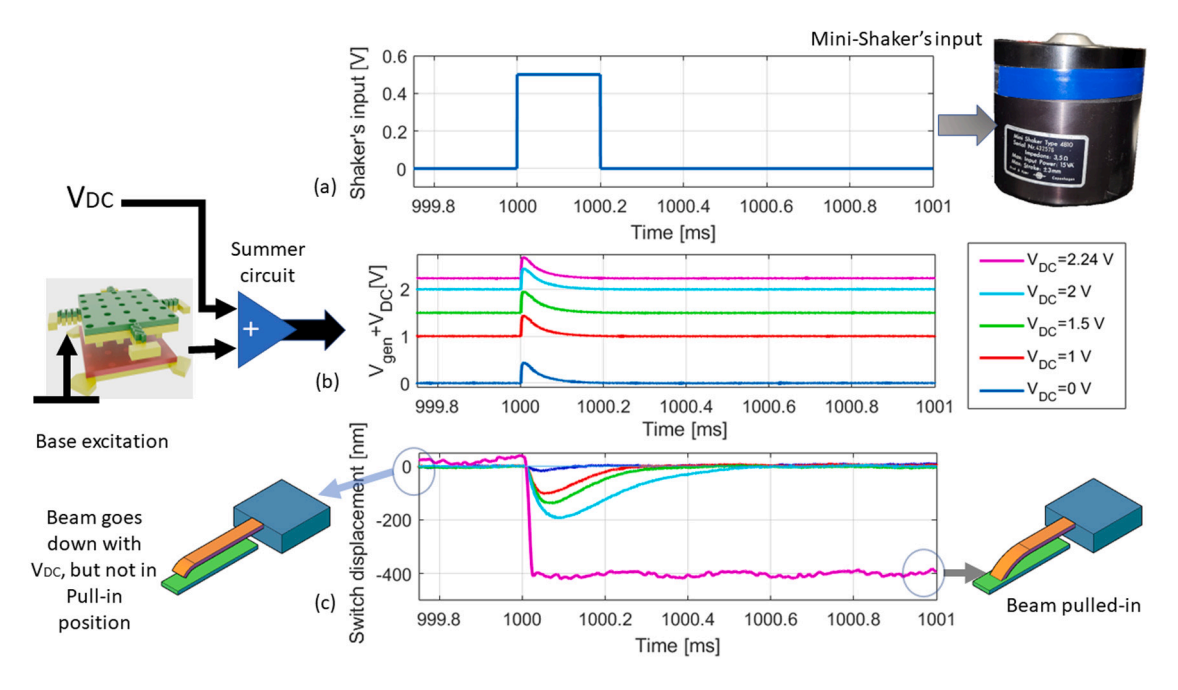


Fig. 7. (a) impulse input to the shaker and summer's output, (b) displacement of the beam measured from the steady-state response of V_{DC} , (c) initial position of the switch before the shock and V_{DC} are applied, (d) the switch position after V_{DC} was applied (curved down but still open), and (e) switch position after the shock was applied.

Table 2
Summary on previous TEGs.

Ref.	Size [cm ³]	Contact area [cm ²]	Gap	Structure	Acc. range	Output	Comments
[59]	4.19	12	~1 cm	Sphere-shaped polyfluoroalkoxy with Aluminum	3.66g	Up to 60V	Crafted manually
[20]	0.2	4	1–8 mm	Cantilever with patterned PDMS	1g	Up to 1.6 V pulses	SU-8 patterned with photolithography
[60]	54	4	1 mm	Layered biocompatible polymers with Aluminum	2.35g	25 V pulses	Patterned with double drawing lithography
[53]	2.27×10^{-4}	0.15	13 μm	C-S Al/Teflon with proof mass of Nickle	9.33g	0.4 V for sinusoidal excitation	UV-LIGA fabrication process used, has over 10 μm top electrode thickness
This work	2.7×10^{-6}	0.0225	1 μm	C-S Al/PI triboelectric pair square layers	between 1.8–2.4g	0.4 V for impulse excitation	Fabricated in MEMS facility, ${\sim}1~\mu m$ top electrode thickness

The generated output from the generator is fed to a summer circuit with a unity gain built using 3 resistors of 100 k Ω and an operational amplifier (OPA177) that is powered by dual-channel power supply (BK-precision). The use of summer is to provide a DC-bias that comes directly from the DAQ, this bias is needed because the switch closes at 2.25 V. The switch is a parallel-plate system with a cantilevered-beam driven by the summers output (Fig. 6c), the switch also has two electrodes to the sides which apply electrostatic force upward to the beam, this helps to release the cantilever beam when it gets stuck after electrostatic pull-in. The displacement of the cantilever is measured using Laser-Doppler-Vibrometer (MSA 500) and the displacement is fed-back to MATLAB through the DAQ.

The Results of supplying a MEMS switch with the MEMS-TENG are shown in Fig. 7. First, a square shock is applied to the electrodynamic mini shaker (Fig. 7a). The output of the MEMS-TENG (V_{Gen}) is summed with DC voltage from the DAQ (V_{DC}) using the summer circuit, the summation output is measured and shown in Fig. 7b for various DC voltages. As a result of the applied voltage the beam curls down relative to that voltage as shown in Fig. 7c. As the DC voltage is applied for 1 s before the shock, the static displacement measured from the Laser-Doppler-Vibrometer is drifted due to the limitation of the phase-shift measurement method the vibrometer used for this measurement.

To avoid the drifted measurement, displacement resulting from the applied DC voltage is ignored before the shock and, thus, the zero displacements is the reference point that enables comparison between displacements caused by the shock as the DC voltage is increased. Because the pull-in voltage of the MEMS switch is 2.25 V and the generated voltage of the generator (V_{Gen}) is an impulse-shaped signal peaking at 0.4 V, a DC voltage (V_{DC}) up to 2.24 V is provided to reach the pull-in after the shock.

In the switching motion shown in Fig. 7c, we notice that the switch is fully open before V_{DC} and the shock are applied in the presence of different V_{DC} s. Once a constant voltage is applied to the switch, the beam curls down toward the pull-in position (switch still open), as the V_{DC} is increased, a larger motion is induced by the same 0.4 V impulse produced from MEMS-TENG as a result of the shock power of 2.1 g. When the applied DC voltage to the MEMS switch increases, its equivalent stiffness decreases and moves easier because of the shock. This parameter acts as a tuning parameter of the MEMS switch. For $V_{DC}=2.24$ V the generated voltage can cause the switch to get closed by driving the MEMS switch to the pull-in instability region. We notice in Fig. 7b that the produced impulse has \sim 0.4 V at peak, however, this signal decays in \sim 200 μ s. Because of this decay, the DC voltage needed

to close the switch is 2.24 V. This voltage is provided by the DAQ and is added to the $V_{\it generated}$ from the shock. If there is no shock, the nominal pull-in voltage of 2.25 V is needed to close the switch.

5. Conclusion

We presented a fabrication process for a contact-separation mode triboelectric generator that can be used for energy harvesting and selfpowered sensing. The generated output is convenient for generating an electrostatic field in micro-scale plates and therefore is applicable for driving MEMS switches. Both components, MEMS-TENG and Switch, are fabricated using the CMOS-compatible microfabrication methods in a cleanroom environment. The micro-sized triboelectric generator reported in this work is smaller than any reported in previous works with 1.5 mm \times 1.5 mm \times 1 μ m top electrode and a gap of 2 μ m. The fabricated device in this work used thin film aluminum and polyimide as a triboelectric pair. The reported triboelectric generator is fabricated with MEMS technology that enables scaling up to high volume production of self-powered MEMS sensors and actuators with low-power demand. The MEMS-TENG was used as a shock detector where the impact resulted in an impulse voltage with 0.4 V peak, this voltage was used as a trigger to close a micro-scale switch.

CRediT authorship contribution statement

Mohammad Alzgool: Micro-Fabrication, Methodology, Conceptualization, Formal analysis, Writing – original draft, Writing – review & editing. Mohammad Mousavi: Formal analysis, validation, Simulations, Writing – original draft, Writing – review & editing. Benyamin Davaji: Methodology, Project administration, Writing – review & editing. Shahrzad Towfighian: Conceptualization, Funding acquisition, Methodology, Project administration, Resources, Writing – review & editing.

Declaration of competing interest

The authors declare that they have no known competing financial interests or personal relationships that could have appeared to influence the work reported in this paper.

Data availability

Data will be made available on request.

Acknowledgments

The authors would like to acknowledge the financial support of the National Science Foundation (NSF), United States of America through Grant #1919608. This work was performed in part at the Cornell NanoScale Science and Technology Facility, United States of America, a member of the National Nanotechnology Coordinated Infrastructure, which is supported by the National Science Foundation (Grant NNCI-2025233). In addition, We are grateful to our colleague Yu Tian for the fruitful discussion.

References

- L. Liu, X. Guo, C. Lee, Promoting smart cities into the 5G era with multi-field Internet of Things (IoT) applications powered with advanced mechanical energy harvesters, Nano Energy 88 (2021) 106304.
- [2] K.R. Wijewardhana, E. Jayaweera, J.-K. Song, Novel electrode design for energy harvesting devices based on liquid-solid contact and enhancement of effective interface area, Nano Energy 96 (2022) 107095.
- [3] L. Liu, Q. Shi, C. Lee, A novel hybridized blue energy harvester aiming at all-weather IoT applications, Nano Energy 76 (2020) 105052.
- [4] I. Jung, J. Choi, H.-J. Park, T.-G. Lee, S. Nahm, H.-C. Song, S. Kim, C.-Y. Kang, Design principles for coupled piezoelectric and electromagnetic hybrid energy harvesters for autonomous sensor systems, Nano Energy 75 (2020) 104921.

[5] L. Fang, Q. Zheng, W. Hou, L. Zheng, H. Li, A self-powered vibration sensor based on the coupling of triboelectric nanogenerator and electromagnetic generator, Nano Energy (2022) 107164.

- [6] X. Zhang, J. Ai, Y. Yue, Y. Shi, R. Zou, B. Su, Anti-stress ball energy harvester, Nano Energy 90 (2021) 106493.
- [7] Q. Li, S. Li, D. Pisignano, L. Persano, Y. Yang, Y. Su, On the evaluation of output voltages for quantifying the performance of pyroelectric energy harvesters, Nano Energy 86 (2021) 106045.
- [8] S.-H. Shin, J.Y. Cheong, H. Lim, V.V. Padil, A. Venkateshaiah, I.-D. Kim, Carbon anchored conducting polymer composite linkage for high performance water energy harvesters, Nano Energy 74 (2020) 104827.
- [9] Y. Zhang, T. Wang, A. Luo, Y. Hu, X. Li, F. Wang, Micro electrostatic energy harvester with both broad bandwidth and high normalized power density, Appl. Energy 212 (2018) 362–371.
- [10] J. Wang, S. Zhou, Z. Zhang, D. Yurchenko, High-performance piezoelectric wind energy harvester with Y-shaped attachments, Energy Convers. Manage. 181 (2019) 645–652.
- [11] K. Chen, Q. Gao, S. Fang, D. Zou, Z. Yang, W.-H. Liao, An auxetic nonlinear piezoelectric energy harvester for enhancing efficiency and bandwidth, Appl. Energy 298 (2021) 117274.
- [12] L. Yan, Y. Mi, Y. Lu, Q. Qin, X. Wang, J. Meng, F. Liu, N. Wang, X. Cao, Weaved piezoresistive triboelectric nanogenerator for human motion monitoring and gesture recognition, Nano Energy 96 (2022) 107135.
- [13] W. Tian, Z. Ling, W. Yu, J. Shi, A review of MEMS scale piezoelectric energy harvester, Appl. Sci. 8 (4) (2018) 645.
- [14] M. Khazaee, A. Rezaniakolaie, L. Rosendahl, A broadband macro-fiber-composite piezoelectric energy harvester for higher energy conversion from practical wideband vibrations, Nano Energy 76 (2020) 104978.
- [15] Z. Li, L. Tang, W. Yang, R. Zhao, K. Liu, B. Mace, Transient response of a nonlinear energy sink based piezoelectric vibration energy harvester coupled to a synchronized charge extraction interface, Nano Energy 87 (2021) 106179.
- [16] W.-G. Kim, J.-K. Kim, D.-W. Kim, I.-W. Tcho, Y.-K. Choi, A triboelectric nanogenerator implemented with an acoustic foam for a self-driven silent tire, Nano Energy 96 (2022) 107090.
- [17] D. Chen, S. Hao, C. Xu, L. Liu, L. Zhao, H. Hong, W. Xu, Q. Tang, X. Du, X. Yang, In-situ high-efficiency PM capture from motor vehicle exhaust based on self-powered ceramic porous triboelectric filter, Nano Energy 96 (2022) 107107.
- [18] S. Shi, Y. Jiang, Q. Xu, J. Zhang, Y. Zhang, J. Li, Y. Xie, Z.-P. Cao, A self-powered triboelectric multi-information motion monitoring sensor and its application in wireless real-time control, Nano Energy (2022) 107150.
- [19] X. Zhang, J. Zhao, X. Fu, Y. Lin, Y. Qi, H. Zhou, C. Zhang, Broadband vibration energy powered autonomous wireless frequency monitoring system based on triboelectric nanogenerators, Nano Energy (2022) 107209.
- [20] L. Dhakar, F.E.H. Tay, C. Lee, Development of a broadband triboelectric energy harvester with SU-8 micropillars, J. Microelectromech. Syst. 24 (1) (2014) 91–99.
- [21] S. Dai, X. Li, C. Jiang, Q. Zhang, B. Peng, J. Ping, Y. Ying, Omnidirectional wind energy harvester for self-powered agro-environmental information sensing, Nano Energy 91 (2022) 106686.
- [22] X.-S. Zhang, M. Han, B. Kim, J.-F. Bao, J. Brugger, H. Zhang, All-in-one self-powered flexible microsystems based on triboelectric nanogenerators, Nano Energy 47 (2018) 410–426.
- [23] H. Chen, Y. Song, X. Cheng, H. Zhang, Self-powered electronic skin based on the triboelectric generator, Nano Energy 56 (2019) 252–268.
- [24] Q. Tang, H. Guo, P. Yan, C. Hu, Recent progresses on paper-based triboelectric nanogenerator for portable self-powered sensing systems, EcoMat 2 (4) (2020) 112060.
- [25] S.-B. Jeon, W.-G. Kim, S.-J. Park, I.-W. Tcho, I.-K. Jin, J.-K. Han, D. Kim, Y.-K. Choi, Self-powered wearable touchpad composed of all commercial fabrics utilizing a crossline array of triboelectric generators, Nano Energy 65 (2019) 103994
- [26] Y. Wu, Y. Hu, Z. Huang, C. Lee, F. Wang, Electret-material enhanced triboelectric energy harvesting from air flow for self-powered wireless temperature sensor network, Sensors Actuators A 271 (2018) 364–372.
- [27] K. Xia, Z. Zhu, H. Zhang, Z. Xu, A triboelectric nanogenerator as self-powered temperature sensor based on PVDF and PTFE, Appl. Phys. A 124 (8) (2018) 1–7.
- [28] J.-G. Sun, T.-N. Yang, C.-Y. Wang, L.-J. Chen, A flexible transparent onestructure tribo-piezo-pyroelectric hybrid energy generator based on bio-inspired silver nanowires network for biomechanical energy harvesting and physiological monitoring, Nano Energy 48 (2018) 383–390.
- [29] Z. Yu, Y. Zhang, Y. Wang, J. Zheng, Y. Fu, D. Chen, G. Wang, J. Cui, S. Yu, L. Zheng, et al., Integrated piezo-tribo hybrid acoustic-driven nanogenerator based on porous MWCNTs/PVDF-TrFE aerogel bulk with embedded PDMS tympanum structure for broadband sound energy harvesting, Nano Energy (2022) 107205.
- [30] H. Patnam, S.A. Graham, J.S. Yu, Y-ZnO microflowers embedded polymeric composite films to enhance the electrical performance of piezo/tribo hybrid nanogenerators for biomechanical energy harvesting and sensing applications, ACS Sustain. Chem. Eng. 9 (12) (2021) 4600–4610.
- [31] G. Luo, Q. Zhang, M. Li, K. Chen, W. Zhou, Y. Luo, Z. Li, L. Wang, L. Zhao, K.S. Teh, et al., A flexible electrostatic nanogenerator and self-powered capacitive sensor based on electrospun polystyrene mats and graphene oxide films, Nanotechnology 32 (40) (2021) 405402.

[32] J. Hillenbrand, P. Pondrom, G. Sessler, Electret transducer for vibration-based energy harvesting, Appl. Phys. Lett. 106 (18) (2015) 183902.

- [33] Z. Wu, M. Bi, Z. Cao, S. Wang, X. Ye, Largely enhanced electrostatic generator based on a bipolar electret charged by patterned contact micro-discharge and optimized substrates, Nano Energy 71 (2020) 104602.
- [34] S.H. Daneshvar, M. Maymandi-Nejad, M. Sachdev, J.-M. Redouté, A charge-depletion study of an electrostatic generator with adjustable output voltage, IEEE Sens. J. 19 (3) (2018) 1028–1039.
- [35] Y. Naito, K. Uenishi, Electrostatic MEMS vibration energy harvesters inside of tire treads, Sensors 19 (4) (2019) 890.
- [36] X. Mo, H. Zhou, W. Li, Z. Xu, J. Duan, L. Huang, B. Hu, J. Zhou, Piezoelectrets for wearable energy harvesters and sensors, Nano Energy 65 (2019) 104033.
- [37] X. Xu, Y. Wang, P. Li, W. Xu, L. Wei, Z. Wang, Z. Yang, A leaf-mimic rain energy harvester by liquid-solid contact electrification and piezoelectricity, Nano Energy 90 (2021) 106573.
- [38] Y. Sun, J. Chen, X. Li, Y. Lu, S. Zhang, Z. Cheng, Flexible piezoelectric energy harvester/sensor with high voltage output over wide temperature range, Nano Energy 61 (2019) 337–345.
- [39] J. Kim, S. Byun, S. Lee, J. Ryu, S. Cho, C. Oh, H. Kim, K. No, S. Ryu, Y.M. Lee, et al., Cost-effective and strongly integrated fabric-based wearable piezoelectric energy harvester, Nano Energy 75 (2020) 104992.
- [40] B. Wang, Z. Long, Y. Hong, Q. Pan, W. Lin, Z. Yang, Woodpecker-mimic twolayer band energy harvester with a piezoelectric array for powering wrist-worn wearables, Nano Energy 89 (2021) 106385.
- [41] J. Kan, W. Liao, J. Wang, S. Wang, M. Yan, Y. Jiang, Z. Zhang, Enhanced piezoelectric wind-induced vibration energy harvester via the interplay between cylindrical shell and diamond-shaped baffle, Nano Energy 89 (2021) 106466.
- [42] S. Maiti, S.K. Karan, J.K. Kim, B.B. Khatua, Nature driven biopiezoelectric/triboelectric nanogenerator as next-generation green energy harvester for smart and pollution free society, Adv. Energy Mater. 9 (9) (2019) 1802027
- [43] W. Kim, J.H. Park, H.J. Hwang, Y.S. Rim, D. Choi, Interfacial molecular engineering for enhanced polarization of negative tribo-materials, Nano Energy 96 (2022) 107110.
- [44] S.-J. Park, S. Lee, M.-L. Seol, S.-B. Jeon, H. Bae, D. Kim, G.-H. Cho, Y.-K. Choi, Self-sustainable wind speed sensor system with omni-directional wind based triboelectric generator, Nano Energy 55 (2019) 115–122.
- [45] D. Park, J.-H. Hong, D. Choi, D. Kim, W.H. Jung, S.S. Yoon, K.H. Kim, S. An, Biocompatible and mechanically-reinforced tribopositive nanofiber MAT for wearable and antifungal human kinetic-energy harvester based on wood-derived natural product, Nano Energy 96 (2022) 107091.
- [46] S.K. Karan, S. Maiti, J.H. Lee, Y.K. Mishra, B.B. Khatua, J.K. Kim, Recent advances in self-powered tribo-/piezoelectric energy harvesters: all-in-one package for future smart technologies, Adv. Funct. Mater. 30 (48) (2020) 2004446.
- [47] Y. Song, N. Wang, C. Hu, Z.L. Wang, Y. Yang, Soft triboelectric nanogenerators for mechanical energy scavenging and self-powered sensors, Nano Energy 84 (2021) 105919.
- [48] R. Bogue, Recent developments in MEMS sensors: A review of applications, markets and technologies, Sensor Rev. (2013).
- [49] M. Mousavi, M. Alzgool, S. Towfighian, Autonomous shock sensing using bistable triboelectric generators and MEMS electrostatic levitation actuators, Smart Mater. Struct. 30 (6) (2021) 065019.
- [50] M. Pallay, A.I. Ibrahim, R.N. Miles, S. Towfighian, Pairing electrostatic levitation with triboelectric transduction for high-performance self-powered MEMS sensors and actuators, Appl. Phys. Lett. 115 (13) (2019) 133503.
- [51] C. Chen, Z. Wen, J. Shi, X. Jian, P. Li, J.T. Yeow, X. Sun, Micro triboelectric ultrasonic device for acoustic energy transfer and signal communication, Nature Commun. 11 (1) (2020) 1–9.
- [52] H.A. Hamid, Z. Celik-Butler, Design and optimization of a MEMS triboelectric energy harvester for nano-sensor applications, in: 2019 IEEE Sensors Applications Symposium, SAS, IEEE, 2019, pp. 1–6.
- [53] H.A. Hamid, Z. Çelik-Butler, A novel MEMS triboelectric energy harvester and sensor with a high vibrational operating frequency and wide bandwidth fabricated using UV-LIGA technique, Sensors Actuators A 313 (2020) 112175.
- [54] G. Turban, M. Rapeaux, Dry etching of polyimide in O 2-CF 4 and O 2-SF 6 plasmas, J. Electrochem. Soc. 130 (11) (1983) 2231.
- [55] M. Daeichin, R.N. Miles, S. Towfighian, Large-stroke capacitive MEMS accelerometer without pull-in, IEEE Sens. J. 21 (3) (2020) 3097–3106.

- [56] S. Niu, S. Wang, L. Lin, Y. Liu, Y.S. Zhou, Y. Hu, Z.L. Wang, Theoretical study of contact-mode triboelectric nanogenerators as an effective power source, Energy Environ. Sci. 6 (12) (2013) 3576–3583.
- [57] A. Ibrahim, A. Ramini, S. Towfighian, Experimental and theoretical investigation of an impact vibration harvester with triboelectric transduction, J. Sound Vib. 416 (2018) 111–124.
- [58] S. Li, Y. Fan, H. Chen, J. Nie, Y. Liang, X. Tao, J. Zhang, X. Chen, E. Fu, Z.L. Wang, Manipulating the triboelectric surface charge density of polymers by low-energy helium ion irradiation/implantation, Energy Environ. Sci. 13 (3) (2020) 896–907.
- [59] H. Zhang, Y. Yang, Y. Su, J. Chen, K. Adams, S. Lee, C. Hu, Z.L. Wang, Triboelectric nanogenerator for harvesting vibration energy in full space and as self-powered acceleration sensor, Adv. Funct. Mater. 24 (10) (2014) 1401–1407.
- [60] H. Wang, Z. Xiang, P. Giorgia, X. Mu, Y. Yang, Z.L. Wang, C. Lee, Triboelectric liquid volume sensor for self-powered lab-on-chip applications, Nano Energy 23 (2016) 80–88.



Mohammad Alzgool received B.Sc. degree in Biomedical engineering and MS degree in Mechanical engineering from Jordan University of Science and Technology. He has been a Ph.D. student since 2019 in State University of New York at Binghamton. His areas of interest include MEMS sensors and actuators, modeling, and MEMS fabrication.



Mohammad Mousavi received his M.Sc. in Mechanical Engineering from the University of Tehran, Iran in 2017. Since 2019, he has started his Ph.D. in Mechanical Engineering department at Binghamton University. His research interests include simulation, dynamic analysis, and motion control of MEMS sensors and actuators. He also focuses on triboelectric generators and energy harvesting.



Benyamin Davaji joined Northeastern Engineering in January 2022 as an assistant professor in the Electrical and Computer Engineering Department. He received his Ph.D. degree in Electrical and Computer Engineering from Marquette University in 2016, and held a post-doctoral associate position in Electrical and Computer Engineering at Cornell University. His main research interests include integrated microsystems emphasizing sensing and computation using mechanical waves, acoustic/ultrasound transducers, bio-interfaces, microcalorimetry, and implementing dataguided methods for system design, nanofabrication, and semiconductor manufacturing.



Shahrzad Towfighian received her Ph.D. degree in Mechanical Engineering from the University of Waterloo, Canada in 2011. She joined the Mechanical Engineering department at Binghamton University in Fall 2013. Her research interests include Micro-electro-mechanical sensors/actuators and energy harvesting. She develops mathematical models and experimental platforms to study electro-mechanical systems and their coupled interactions. She discovers new ways of sensing and actuation for improving functionality of micro-scale devices.